Outer Heliospheric Turbulence and the Angular Broadening of Radio Sources from the Voyager Data

Journal of Physics: Conference Series **1620** (2020) 012022 doi:10.1088/1742-6596/1620/1/012022

Outer Heliospheric Turbulence and the Angular Broadening of Radio Sources from the Voyager Data

Samira Tasnim[1], Gary P. Zank[1], Iver H. Cairns[2], and L. Adhikari[1]

[1] Center for Space Plasma and Aeronomic Research (CSPAR), University of Alabama in Huntsville, Huntsville, AL 35805, USA

[2] School of Physics, The University of Sydney, NSW-2006, Australia

E-mail: samira.tasnim@uah.edu, garyp.zank@gmail.com, iver.cairns@sydney.edu.au, laxman.adhikari@uah.edu

Abstract. The properties of density turbulence are important in estimating the angular broadening of radio sources in the outer heliosphere and very local interstellar medium (VLISM). We calculate the density variance, inner scale, correlation length of the velocity, and relative density amplitude as a function of radial distance using plasma and magnetometer data from the Voyager 2 spacecraft over the period 1977 to 2018. We apply three different techniques to estimate the density turbulence amplitude, including an inner scale, using the Voyager 2 data. Related analyses compare Voyager data determined turbulence amplitudes with results from the density turbulence theories of Zank et al. [49, 50] and Bellamy et al. [6]. Theoretical predictions and observations show strong similarities: both qualitatively and quantitatively. In addition, the predicted turbulence amplitudes show radial trends similar to those observed. The numerical prediction of the scattering angle uses a turbulence spectrum that includes an inner scale. The numerical and analytic results are compared, and we find similar radial trends.

1. Introduction

An important observation of the Voyager missions was the detection of low-frequency radio waves that are apparently generated in one or more of the regions where the solar wind interacts with the interstellar medium [4, 18, 20, 26–28, 32, 33, 45]. Both Voyager 1 and 2 observed radio events while they were separated by a distance of more than 40 AU [26, 28]. Existing theories predict that the source of these radio events was at a very large distance, probably in the very local interstellar medium [14, 17, 19, 27, 28, 47, 48]. Here, we use the definition of the very local interstellar medium (VLISM) introduced by Zank [47].

The Voyager spacecraft regularly calibrates the magnetometer using roll maneuvers. It was observed during these roll maneuvers that the intensity of the outer heliospheric radiation close to 3 kHz is modulated. Later, Kurth [32], Gurnett et al. [27, 28], Cairns [12, 13], and Armstrong et al. [4] interpreted this modulation in terms of the apparent size and direction to the radiation source. However, 2 kHz radiation did not show this modulation which was interpreted by Armstrong et al. [4] as meaning that the location of the source was exactly along the roll axis or that the radiation was isotropic. Gurnett et al. [27] associated the global merged interaction regions (GMIRs) with the radio emission observed by the Voyager 1 and 2 spacecraft, which then yields a corresponding timing between a Forbush decrease observed in the heliosphere and the subsequent turn-on of radiation. This raises the question of how the radio emission propagates

to the Voyager spacecraft through and around the GMIRs, and associated shock moving up a density ramp at the heliopause and beyond (e.g., the density depletion layer [16]). Radiation generated close to either the electron plasma frequency f_p or $2f_p$ cannot propagate through the enhanced density of a GMIR [5, 13, 15, 19, 23, 25].

All analyses of radiation generated near f_p and $2f_p$ in the solar wind between the corona and 1 AU demonstrate that scattering by density turbulence plays an important role in the angular broadening, brightness temperature, and the direction of propagation [13, 30, 38, 39, 41]. Indeed, the scattering of radio waves throughout the solar system and in any astrophysical plasmas is strongly mediated by density irregularities, affecting the radio waves' intensity, angular size, direction, and temporal and spectral variability [14, 36, 38, 39]. Accordingly, the amplitudes and spatial scales of density turbulence are important in estimating the angular broadening of radio sources in the outer heliosphere or very local interstellar medium (VLISM) [4, 13, 14, 45].

Cairns [12, 13] argued that scattering by density irregularities in the outer heliosphere leads to a significant angular broadening of the 2 - 3 kHz radiation and may also change the apparent direction of the source. Cairns [13] found reasonable agreement of the angular broadening inferred from roll maneuvers and a model that extrapolated the amplitude and the Kolmogorov properties of density turbulence from within 1 AU to the outer heliosphere, ignored inner scale effects, and reduced the scattering by a factor $w = 0.01$. However, the introduction of the factor w suggests that these investigations did not account for some potentially important physical processes. For instance, (i) the inner scale, which ensures that turbulence does not extend to infinitely small spatial scales, has significant effects on radio wave scattering by density fluctuations [4, 14, 31, 38]; (ii) the radial dependence of the fluctuating density variance may be different outside and inside 1 AU [2]; and (iii) the density variance in the equatorial plane is nearly 16 times stronger than in the polar regions [4, 22]. Note that various investigations [4, 22, 31] of angular broadening of radio sources in the corona and solar wind use different definitions of the inner (dissipation) scale.

Here, we extend the analysis of Cairns [13, 14] to address the three points described above. Our paper is structured as follows. Section 2 presents a power spectral analysis to determine the observed density turbulence amplitude, which includes the correlation length, and the inertial range, and we introduce a definition of the inner scale as a function of wave number. Section 3 briefly describes the parabolic wave equation theory and the angular broadening of radio sources. Section 4 presents the Voyager 2 data. Section 5 compares observations with analytic predictions, and we conclude with a brief discussion in Section 6.

2. Theories to Estimate the Amplitude of Turbulence

We employ three different approaches to estimate the amplitude of density turbulence in the heliosphere. For convenience, we identify them as model 1, model 2, and model 3. We briefly describe the models in the following subsections.

2.1. Model 1 : Employing Theories by Coles et al. [22] and Lee and Jokipii [36]

Density turbulence can be modeled using a three dimensional isotropic spatial power spectrum that has a power-law component, an exponential cutoff at an inner scale, and an amplitude that varies with radial distance R [22, 36, 38, 39], according to

$$S_n(\mathbf{k}, \mathbf{R}) = \langle (\delta\rho)^2 \rangle (\mathbf{k}, \mathbf{R}) = C_N^2(R) k^{-\alpha} \exp^{-(kl_i/2\pi)^2}, \tag{1}$$

where $\mathbf{k}$ denotes wave vector, $|\mathbf{k}| = k$, and

$$\langle (\delta\rho)^2 \rangle (\mathbf{R}) = \int_{k_{min}}^{k_{max}} d^3\mathbf{k} \langle (\delta\rho)^2 \rangle (\mathbf{k}, \mathbf{R}) \simeq k^3 \langle (\delta\rho)^2 \rangle (\mathbf{k}, \mathbf{R}). \tag{2}$$

Here $\langle(\delta\rho)^2\rangle$ is the fluctuating density variance, C_N^2 is the amplitude of the density turbulence, l_i is the inner scale, and $\alpha = 11/3$ corresponds to choosing the three dimensional Kolmogorov spectrum. Equations (1) and (2) yield

$$C_N^2(R) = k^{\alpha-3}\langle(\delta\rho)^2\rangle(\mathbf{R})\exp^{(kl_i/2\pi)^2}. \tag{3}$$

We assume here that the inner scale is a free parameter. Zank et al. [49] show that the density variance $\langle(\delta\rho)^2\rangle$ behaves as a passive scalar in response to turbulent velocity fluctuations and that the decay rate is governed by the velocity correlation length l_u. On assuming a Kolmogorov phenomenology, Zank et al. [49] show that the wave number spectrum for the density variance is $k^{-5/3}$ in the solar wind. The inertial range extends roughly over three decades and is bounded by wave numbers corresponding to approximately l_u^{-1} and l_i^{-1}. A crude range of $\sim 10^{-2} - 10^{-3}$ separates l_u and l_i in the solar wind, i.e. $l_i/l_u \sim 10^{-2} - 10^{-3}$ (e.g. Bruno and Carbone [7]). Coles et al. [22] and Ingale et al. [31] suggest that the inner scale arises from cyclotron damping, and should be comparable to the thermal proton gyro-radius $r_{pg} = (m_p v_p)/(q_p B)$. In modeling the inner scale, we assume

$$l_i = \beta l_u, \tag{4}$$

provided $\beta l_u > r_{pg}$ and β is chosen as 10^{-2}. Otherwise, we take $l_i \sim r_{pg}$ for a locally thermal proton, specifically,

$$l_i = 2\pi r_g = \frac{2\pi m_p v_p}{q_p B}. \tag{5}$$

Here m_p and q_p are the mass and charge of a proton, B is the magnetic field magnitude at R, $v_p = \sqrt{(K_B T_p)/m_p}$ is the proton thermal velocity, K_B is the Boltzmann constant, and T_p is the thermal proton temperature.

2.2. Model 2: Employing Zank et al. [49]'s Turbulence Transport Theory
The variance of isotropic density turbulence from Zank et al. [49] is

$$\langle(\delta\rho)^2(R)\rangle = \int E_p dk_\perp \approx E_p(k_\perp)k_\perp, \tag{6}$$

where E_p is the variance of density fluctuations/wave number and $k_\perp$ is a perpendicular wave number.

Figure 1 shows the wave number $k_\perp^u$ that separates the energy-containing range and the inertial range. Therefore, at $k_\perp^u$, we can equate the power spectrum distribution at the energy-containing range and the inertial range [3], which yields

$$Ak_\perp^{-1}|_{k_\perp^u} = C_N^2 k_\perp^{-5/3}\exp\left[-\left(\frac{k_\perp l_i}{2\pi}\right)^2\right]_{k_\perp}. \tag{7}$$

By integrating over the power spectrum between the limits k_{inj} to $k_\perp^u$ [3], we find

$$\langle(\delta\rho)^2\rangle(R) = \int_{k_{inj}}^{k_\perp^u} E_p(k_\perp)dk_\perp = A\int_{k_{inj}}^{k_\perp^u} k_\perp^{-1}dk_\perp = A\ln\left(\frac{k_\perp^u}{k_{inj}}\right). \tag{8}$$

Equation (8) gives

$$A = \frac{\langle(\delta\rho)^2\rangle(R)}{\ln\left(\frac{k_\perp^u}{k_{inj}}\right)}, \tag{9}$$

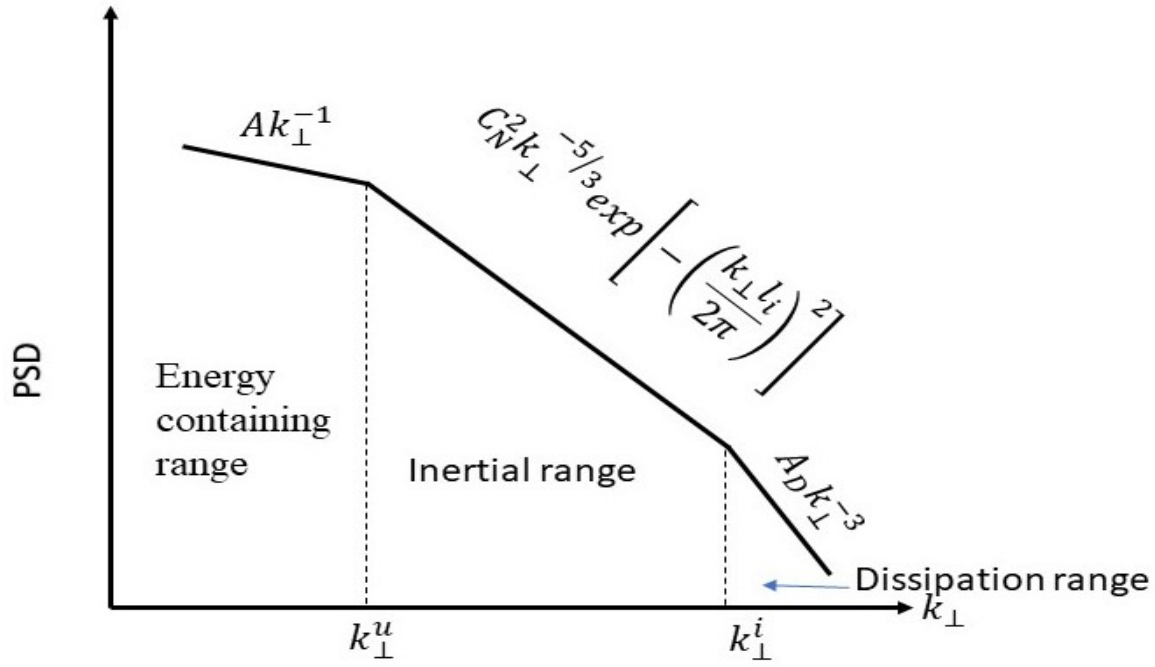

Figure 1. Density power spectrum in the energy containing range, the inertial range, and the dissipation range as a function of wave number [46].

where $k_{inj} \sim 1.07 \times 10^{-6.5}\,\mathrm{km}^{-1}$ is the injection wave number for a solar rotation period and $l_u^\perp$ is the correlation length corresponding to velocity fluctuations in the perpendicular direction. We set, $l_u^\perp = (k_\perp^u)^{-1}$ (neglecting the term of 2π) where $k_\perp^u$ is the wave number that separates the inertial range and the energy containing range. Similarly, the 3D spectrum equation (7) reduces to

$$Ak_\perp^{-3}|_{k_\perp^u} = C_N^2 k_\perp^{-11/3} \exp\left[-\left(\frac{k_\perp l_i}{2\pi}\right)^2\right]_{k_\perp}. \tag{10}$$

Using $k_\perp^u = {l_u^\perp}^{-1}$ along with equations (9) and (10), we get

$$C_N^2(R) = \frac{\langle(\delta\rho)^2\rangle(R) {l_u^\perp}^{-2/3}}{\ln\left(\frac{1}{k_{inj} l_u^\perp}\right) \exp\left[-\left(\frac{l_i}{2\pi l_u^\perp}\right)^2\right]}. \tag{11}$$

Note that we use $l_u^\perp = l_u$ and $k_\perp^u = l_u^{-1}$ for the subsequent analyses.

2.3. Model 3: Employing Bellamy et al. [6]'s semi-quantitative approach

Bellamy et al. [6] analysed the Voyager plasma density data to obtain power spectra, $C_N^2(R)$, and spectral indices as a function of heliocentric radial distance R. In detail, they obtained yearly averages of the temporal power spectrum by Fourier transforming carefully chosen time periods of Voyager density data, averaging and smoothing the individual power spectra for each year, and then fitting the result with a power-law. Associating the resulting spectrum $S_n(f, R_{av})$ for each year with the average value of R, R_{av}, for Voyager 2 that year, they showed that

$$S_n(f, R_{av}) = C_t^2(R_{av}) f^{-\beta_B(R_{av})}, \tag{12}$$

to a good approximation in two ranges of f, where f is the frequency of the data. Bellamy et al. [6] found that the density variance spectrum exhibited dual power-law characteristics: i) the spectral index for frequencies higher than 10^{-4} Hz is close to Kolmogorov ($-5/3$ for 1D spectrum) and ii) the spectral index for the 1D spectrum is ~ -2 for the low frequency regime. Writing R_{av} as R below for convenience, they also found that the indices remain nearly constant with R for both the high and low frequency part of the spectrum until about 30 AU. However, the high frequency spectral index approaches a value close to the Kraichnan value (3/2) beyond 30 AU. We employ here the index of the high frequency component of the density power spectrum. Bellamy et al. [6] converted to the spatially varying wave number power spectrum for an assumed constant solar wind speed $v_{sw} = 400\,\mathrm{kms}^{-1}$ by making the Taylor hypothesis whence

$$C_N^2(R) = (2\pi)^{\alpha} v_{sw}^{(1-\alpha)} C_t^2(R)\rangle, \tag{13}$$

where $\alpha = \beta_B$ [equation (12)] for all data.

3. The Parabolic Wave Equation (PWE) Formalism and Angular Broadening of the Radio Source

Angular broadening due to the scattering of radio waves by density irregularities is calculated by using the parabolic wave equation (PWE) theory [4, 14, 22, 34, 36, 38, 39]. We start with a scalar field u of a locally planar electromagnetic field with wave number k where u is measured in a plane perpendicular to the propagation direction z. We assume electromagnetic radiation propagating along the z axis at a constant frequency ($f = \omega/2\pi$) in a medium which varies on a timescale longer than $1/f$. The wave number $k(z)$ of the radiation, which varies due to changes in the plasma density with $\delta\rho \ll \rho_0$, can be expressed as

$$k(z) = k_0(z) - \frac{1}{2k_0}\frac{(2\pi f_{p0})^2}{c^2}\frac{\delta\rho}{\rho_0}, \tag{14}$$

where $\lambda_{fs} = c/f$ is the free-space wavelength, f_{p0} is the local steady state plasma frequency, $k_0(z) = k_{fs}n(z)$, $k_{fs} = 2\pi/\lambda_{fs}$, $n(z) = [1 - f_{p0}^2/f^2]^{1/2}$ is the refractive index, ρ_0 is the spatially varying and time stationary density, and $\delta\rho$ is the fluctuating turbulent density. Here, $k_0(z)$ does not include the effects of density turbulence.

We use an infinite series of correlation functions or moments over the scalar field u that contain the statistical information [14, 36]:

$$\Gamma_{1,1}(z, k_0, k_1, \mathbf{s}) = \langle u(z, k_0, \mathbf{s}) u^*(z, k_1, 0)\rangle, \tag{15}$$

where $\Gamma_{1,1}(z, k_0, k_1, \mathbf{s})$ is the variance that describes the pulse broadening of the radiation, the angle brackets denote an ensemble average of u, $\mathbf{s}$ is a position vector in the transverse plane, k_0 and k_1 are the wave numbers, and for homogeneous density turbulence $k_1 = k_0$. We use the notation of Lee and Jokipii [36], Lee [35], and Cairns [14].

The angular spectrum $P(\theta, k_0)$ of the radiation can be expressed in terms of the Fourier transformation of the spatial correlation function [14, 36] as

$$P(\boldsymbol{\theta}, k_0) = \frac{k_0^2}{4\pi^2}\int d^2\mathbf{s}\Gamma_{1,1}(z, k_0, k_0, \mathbf{s}) e^{-\mathbf{k_0}\cdot\mathbf{s}}, \tag{16}$$

where $\boldsymbol{\theta}$ is the angular wave vector of the radiation. The inverse Fourier transform of equation (16) yields

$$\Gamma_{1,1}(z, k_0, k_0, \mathbf{s}) = \int d^2\boldsymbol{\theta} P(\theta) e^{ik_0\boldsymbol{\theta}\cdot\mathbf{s}}. \tag{17}$$

A Markov approximation can be used to reduce the scintillation problem in a simple way [36], and eliminates the need to assume Gaussian statistics. The correlation functions $\Gamma_{1,1}(z, k_0, k_0, s)$ in the Markov approximation for an homogeneous turbulent quantity (density fluctuation $\delta\rho$) in the transverse direction [14, 36] can be written as

$$\frac{\partial\Gamma_{1,1}}{\partial z}(z, k_0, k_0, \mathbf{s}) = -r_e^2\lambda_{fs}^2 \frac{1}{(1 - f_{p0}^2/f^2)}\Big[A(z, 0 - A(z, \mathbf{s}))\Big]\Gamma_{1,1}, \tag{18}$$

where f is the radio frequency (2 kHz or 3 kHz) and r_e is the classical electron radius. The transverse correlation function $A(z, \mathbf{s})$, meaning transverse to the propagation path, for the density turbulence is [36]

$$A(z, \mathbf{s}) = 2\pi \int d^2\mathbf{q} P_{3N}(z, 0, -\mathbf{q}) \exp[i\mathbf{q} \cdot \mathbf{s}], \tag{19}$$

after applying a two-dimensional (2D) Fourier transformation [14]. $P_{3N}(z, k_z, \mathbf{q})$ is the three-dimensional density power spectrum and $\mathbf{q}$ denotes the wave vector transverse to the propagation path. We set the transverse wave number $k_z = 0$. Recall, we take z to be the propagation direction of the radio wave. The location of the source is at $z = 0$ and the observer is at $z = z_{ob}$.

By employing a moment analysis of the PWE equation, which includes a spatially varying local plasma frequency $f_{p0}(z)$ [14], coupled with the Markov approximation [14, 36], we obtain the path integral of equation (18) as

$$\Gamma_{1,1}(z, k_0, k_0, \mathbf{s}) = \exp\left[-r_e^2{\lambda_{fs}}^2 \times \int_0^{z_{ob}} dz \frac{2}{\left(1 - \frac{f_{p0}^2(z)}{f^2}\right)}[A(z, 0) - A(z, s)]\right]. \tag{20}$$

Expression (20) includes a spatially varying local plasma frequency $f_{p0}(z)$ [14] and the function $\Gamma_{1,1}(z, k_0, k_0, \mathbf{s})$ describes the angular broadening. Equation (20) can be re-written as

$$\Gamma_{1,1}(z, k_0, k_0, \mathbf{s}) = \exp\left[-D_\phi(z, k_0, s)/2\right], \tag{21}$$

and D_ϕ is known as the phase structure function.

We follow the theoretical model of Cairns [14] and include an inner scale in the 3D density variance spectrum

$$P_{3N}(q, 0, z) = C_N^2(z)(q^2)^{(-\frac{\alpha}{2})}\exp\left[\frac{q}{q_i}\right], \tag{22}$$

where $q_i = (l_i)^{-1}$. Using equations (19), (20), and (22), we derive

$$\Gamma_{1,1}(z, k_0, k_0, \mathbf{s}) = \Gamma_{1,1}(z, 0)\exp\left[-{r_e}^2{\lambda_{fs}}^2\mathbf{s}^{(\alpha-2)}4\pi^2 \int_0^{z_{ob}} dz \frac{C_N^2(z)}{\left(1-\frac{f_{p0}^2(z)}{f^2}\right)} \frac{\Gamma(2-\frac{\alpha}{2})2^{2-\alpha}}{\Gamma(\frac{\alpha}{2})(\alpha-2)} q_i^{(4-\alpha)}\right]. \tag{23}$$

Previous analyses [14, 30, 34, 36, 38] show that the correlation function, and so via equation (16) the angular distribution, becomes Gaussian for Gaussian distributed density turbulence, with

$$P_{3N}(\theta, z) = \frac{1}{\pi\theta_{SC}^2}\exp\left[-\theta^2/\theta_{SC}^2\right], \tag{24}$$

with $\theta^2_{sc}(z) = \langle\theta^2(z)\rangle$. Equating equations (16) and (24) at the half power point and inserting equation (23) for $\Gamma_{1,1}(k_0, z)$, one finds [14] the mean-square scattering angle to be

$$\theta^2_{SC}(z) = \pi^{-2}\left[4\pi^2 r_e^2 \int_0^{z_{ob}} dz \frac{C_N^2(z)\lambda_{fs}^{\alpha}}{\left(1 - \frac{f_{p0}^2(z)}{f^2}\right)} \frac{\Gamma\left(2 - \frac{\alpha}{2}\right) 2^{2-\alpha}}{\Gamma\left(\frac{\alpha}{2}\right)(\alpha - 2)} q_i^{(4-\alpha)}\right]^{\frac{2}{\alpha-2}}. \quad (25)$$

The path length integral (25) can be converted easily to an integral over R from the source R_{so} (when $z = 0$) to the observer R_{ob} (when $z = z_{ob}$) and $dz = -dR$. Therefore, equation (25) becomes

$$\theta^2_{SC}(R) = \pi^{-2}\left[4\pi^2 r_e^2 \int_{R_{ob}}^{R_{so}} dR \frac{C_N^2(R)\lambda_{fs}^{\alpha}}{\left(1 - \frac{f_{p0}^2(R)}{f^2}\right)} \frac{\Gamma(2 - \frac{\alpha}{2})2^{2-\alpha}}{\Gamma(\frac{\alpha}{2})(\alpha - 2)} q_i^{(4-\alpha)}\right]^{\frac{2}{\alpha-2}}. \quad (26)$$

We numerically solve integral (26) for models of the density turbulence. In addition, we use the analytic solution of Cairns [13]:

$$\theta^{5/3}_{SC}(R') = B\lambda^{\frac{11}{3}}\left[\frac{2}{A^2 R'} + \frac{1}{A^3}\log\left(\frac{R' - A}{R' + A}\right)\right]_{R_{ob}}^{R_{so}}, \quad (27)$$

after assuming $f_p(R') = f_{p1}/R'$ in steady-state, where f_{p1} is the plasma frequency at 1 AU, R' is the heliocentric distance measured in AU, and $A = f_{p1}/f$ and $B = 7.0 \times 10^{-12}$. In equation (27), we assumed that the turbulence amplitude C_N^2 varies with R as

$$C_N^2(R) = 3.9 \times 10^{15}\left(\frac{R}{R_s}\right)^{-4.00}(\text{meter})^{-20/3}. \quad (28)$$

Cairns [13] also included a quantity w that multiplies the amplitude factor 3.9×10^{15} in equation (28). This is useful for comparing with the observations, with Cairns [13] requiring $w = 10^{-2}$ for approximate agreement with the predictions of Armstrong et al. [4]. Equation (27) then takes the form

$$\theta_{SC} = (w)^{0.6}\left[B\lambda^{\frac{11}{3}}\left[\frac{2}{A^2 R'} + \frac{1}{A^3}\log\left(\frac{R' - A}{R' + A}\right)\right]_{R_{ob}}^{R_{so}}\right]^{0.6}. \quad (29)$$

4. Voyager Data in the Outer Heliosphere, Inner Heliosheath, and Very Local Interstellar Medium

Figure 2 (from top to bottom) displays the solar wind density (ρ), the calculated variance of the density fluctuation $\langle\rho^2\rangle$, the calculated correlation length of the velocity fluctuations (l_u), the solar wind proton temperature (T_i), the solar wind speed (V_{sw}), and the magnetic field magnitude (B) as a function of heliocentric distance. We calculate these quantities using 1-hour resolution data from Voyager 2 over the period October 1, 1977 to December 31, 2018 using the following steps [1, 2, 49, 50].

(i) We consider a sequence of 10 hour intervals of the solar wind density, the solar wind speed, the solar wind temperature, and the magnetic field magnitude. We then calculate the mean of the solar wind density, solar wind temperature, the magnetic field magnitude, and the variance of the solar wind density in each 10 hour interval.

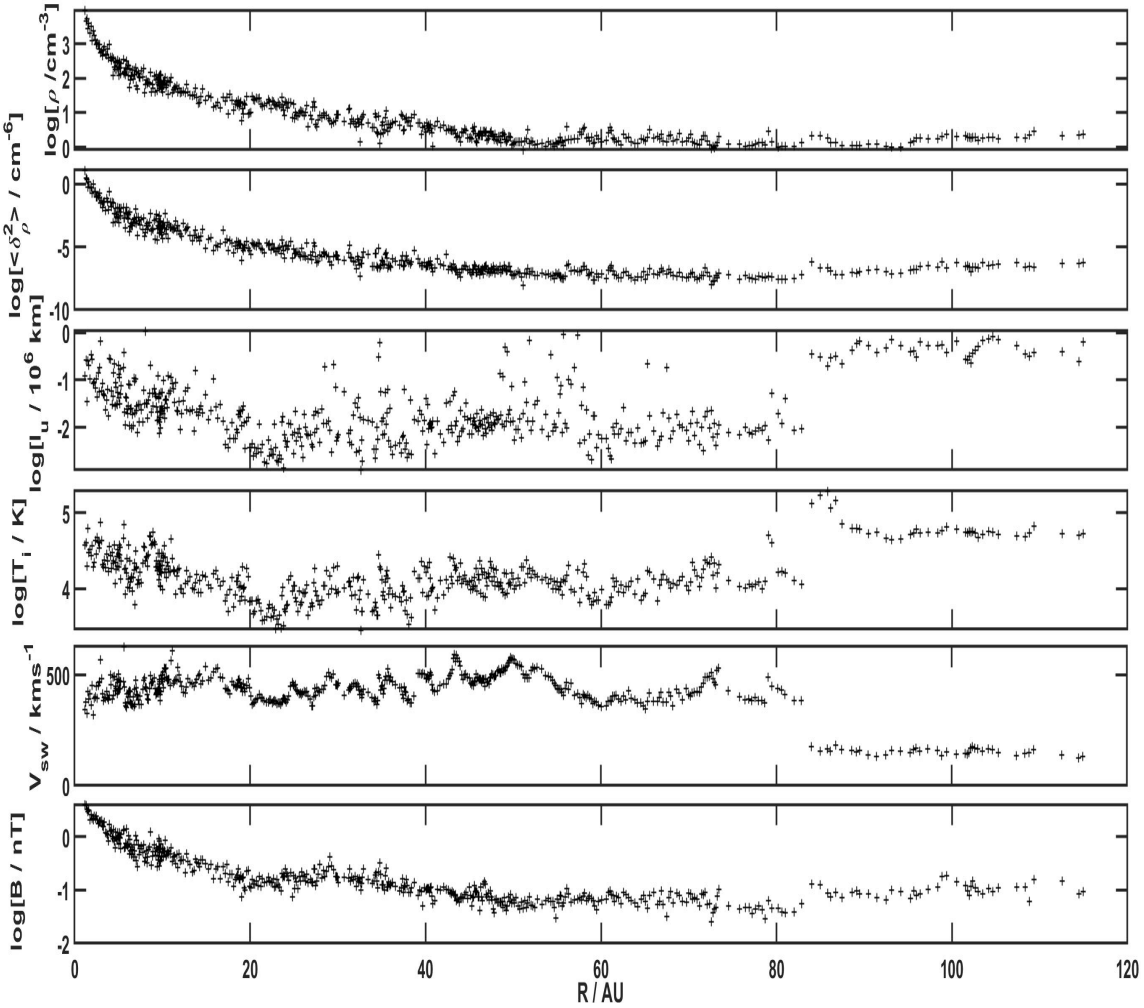

Figure 2. From top to bottom, the density (ρ), fluctuating density variance $\langle(\delta\rho)^2\rangle$, velocity correlation length (l_u), proton temperature (T_i), solar wind speed (V_{sw}), and magnetic field magnitude (B) as a function of radial distance (1 AU to 118 AU) obtained from Voyager 2 data over the period – October 1, 1977 to December 31, 2018.

(ii) Similarly, to calculate the correlation length of the velocity fluctuations, we first calculate the normalized auto-correlation function of solar wind speed as a function of time lag t. The normalized auto-correlation function is 1 at zero time lag t, and decreases with increasing time lag. Using Taylor's hypothesis, the time lag is converted into the spatial lag x.

(iii) The correlation length is calculated by finding the spatial lag r where the normalized auto-correlation function is 1/e of the maximum value. We note that we calculate the mean of the solar wind parameters, the variance of the solar wind density, and the correlation length only if the 10 hour interval contains at least five good data points. Otherwise, we discard the entire interval, and move on to the next interval. We repeat the same process until the end of each yearly Voyager 2 data set.

(iv) Finally, we smooth the data with 23 sequential 10 hour intervals, in which we apply a constraint that the variance of the solar wind density $\langle(\delta\rho)^2\rangle$ must be smaller than the mean

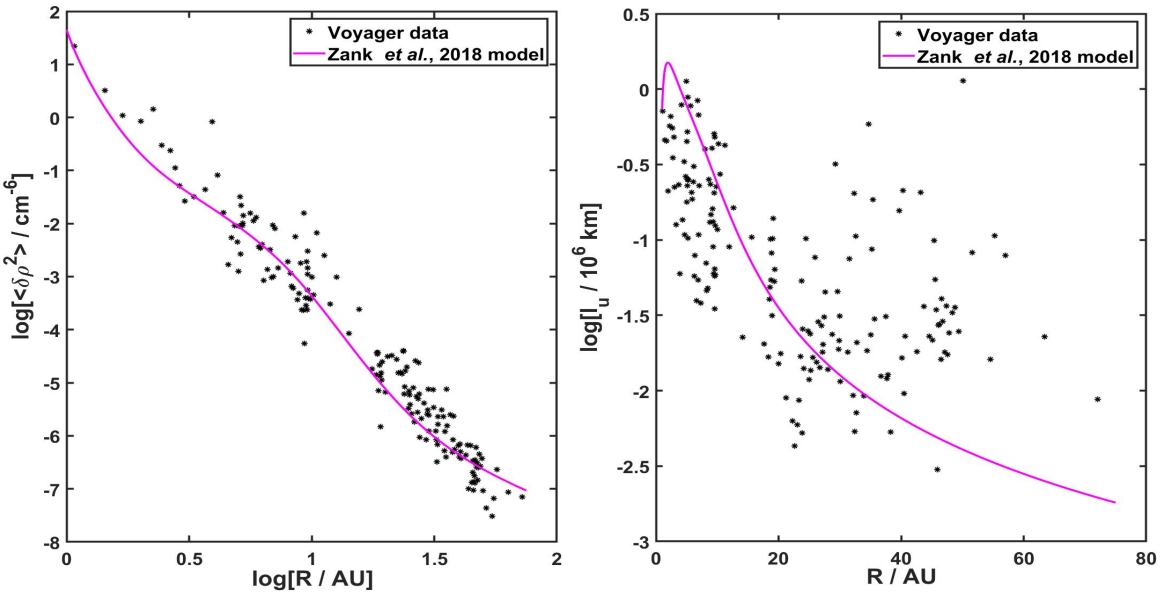

Figure 3. Comparisons between the observed and theoretical values of the fluctuating density variance $\langle(\delta\rho)^2\rangle$ (left) and velocity correlation length l_u (right) using Voyager 2 data and the turbulence transport model of Zank et al. [49], Adhikari et al. [2], and Zank et al. [50].

of the squared solar wind density ($\bar{\rho}^2$), so as to avoid data associated with shocks or any embedded structures within 10 hour intervals. If the data does not meet this condition, we remove the entire row, and average the remaining data for each 10 hour intervals.

Voyager 1 (V1) crossed the heliospheric termination shock (HTS) in December 2004, and Voyager 2 (V2) passed the HTS in August 2007 [42, 43]. V1 and V2 have since crossed the heliopause (HP) and are now traveling through the very local interstellar medium (VLISM) [29, 44]. Figure 2 shows that the HTS was crossed by V2 near 84 AU. Since the Voyager plasma data after 118 AU is quite noisy, we only analyze data observed before December 31, 2018, when V2 reached around 118 AU. Therefore, we assume that the radio source is located no closer than $R_{so} = 118$ AU (i.e. in the VLISM) to numerically solve equation (26). We assume a Kolmogorov-like density turbulence spectrum in the inner heliosheath (IHS) to proceed with our analysis [11].

5. Observations vs Theoretical Predictions

Figure 3 compares the radial profiles of observed and theoretically predicted $\langle(\delta\rho)^2\rangle$ (left panel) and l_u (right panel) using V2 data and the turbulence transport model of Zank et al. [49, 50]. Here we followed the same steps as described in the previous section. However, we select data over 20-hours for steps (i), (ii), (iii), and then smoothed over 10-hour intervals to make a better comparison in step (iv). The left panel exhibits similar radial trends between the observed and the theoretically predicted values. On the other hand, the right panel shows similarities between observations and theoretical predictions of l_u within 30 AU. However, the observed l_u can be larger and is more widely scattered beyond 30 AU, and the comparison is less good.

Figure 4 explores the variation of the inner scale as a function of R. We calculate the inner scale/dissipation scale using equation (4) if $\beta l_u > r_{pg}$, otherwise we use equation (5). The dissipation range (λ_d) is $\sim 2\times10^3$ km [24, 40] and the correlation length (λ_c) is $\sim 10^5$ km [51] at 1

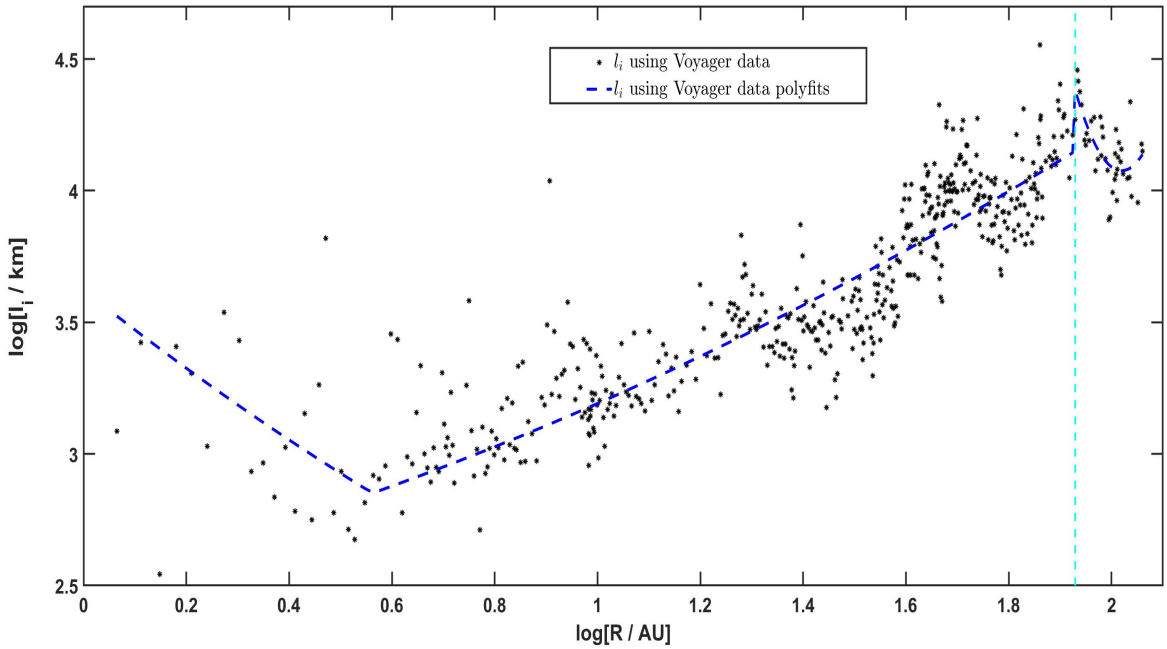

Figure 4. The estimated inner or dissipation scale l_i (black dots $\cdot$ and blue dashes $--$) as a function of heliocentric distance in AU derived from $\beta \times l_u$ and r_{pg} and using V2 data and polyfits to V2 data. We assume $l_i = \beta \times l_u$ when $\beta l_u > r_{pg}$ with $\beta = 10^{-2}$, otherwise, $l_i = 2\pi \times r_{pg}$. Here, the vertical cyan broken line shows the location of HTS.

AU. These observed values of the dissipation and correlation lengths yield the ratio $\lambda_d/\lambda_c \sim 10^{-2}$. Therefore, we assume $\beta = 10^{-2}$ in equation (4). On the other hand, we use $l_i = 2\pi \times r_{pg}$ [i.e. equation (5)] when $\beta l_u < r_{pg}$, as the inner scale l_i should be larger than r_{pg} for thermal protons [22, 31]. However, l_i according to Coles et al. [22] and Ingale et al. [31]'s definition is significantly smaller than βl_u at 1 AU.

In Figure 4, the black dots and broken blue lines display the radial variation of the calculated inner scale derived from V2 data (black dots) and polyfits to the V2 data (blue dashes). We use a second-order polynomial curve fit to estimate the characteristic radial profiles of l_u, T_i, B, and l_i. For convenience, we refer to the fit as a polyfit.

Figure 5 shows the radial variation of C_N^2 from 1 AU to 118 AU. We calculate C_N^2 by fitting data and predictions of Figures 2 and 4 with model 1 [equation (3)] and model 2 [equation (11)]. As for the previous figures, dots and broken lines present direct V2 data and polyfits, respectively. Here, we use polyfits to $\langle(\delta\rho)^2\rangle$, l_u, and l_i from Figure 4 to obtain the polyfits to $C_N^2(R)$ for models 1 and 2. Figure 5 shows similar radial trends with a magnitude difference between predictions of model 1 and model 2. Differences are due to the term $\left[\ln\left(\frac{1}{k_{inj} l_u}\right)\right]^{-1}$ with $k_{inj} \sim 1.07 \times 10^{-6.5}\,\mathrm{km}^{-1}$ that appears in equation (11) unlike equation (3).

Figure 6 compares the turbulence amplitudes predicted by model 1 [equation (3)], model 2 [equation (11)] and model 3 [equation (13)] using the turbulence transport model results of Zank et al. [49, 50] and Voyager data in the outer heliosphere (until 75 AU). We also compare the above results of C_N^2 with analytic predictions by Cairns [13] that used equation (28). Here, equation (28) does not include the w factor. Additionally, we compare predictions from Bellamy et al. [6]. Turbulence downstream of the HTS is likely very different from that upstream, and

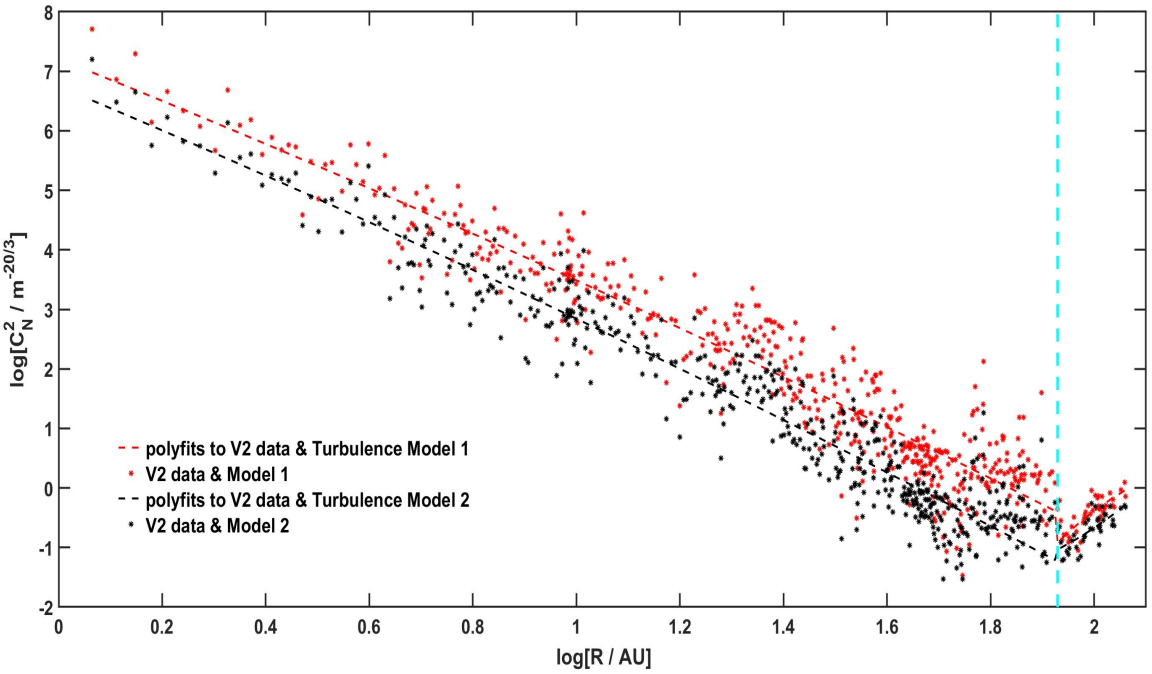

Figure 5. Turbulence amplitude C_N^2 as a function of radial distance from 1 AU to 118 AU derived from polyfits to V2 data [broken lines] and from V2 data itself [scattered dots]. Here the red dots and lines correspond to model 1 and the black dots and lines to model 2. The cyan vertical line indicates the location of the HTS.

almost certainly becomes more compressible [see e.g., Burlaga et al. [10] and Burlaga et al. [11]]. Hence, we do not use the turbulence transport model of Zank et al. [49, 50] in the IHS. Moreover, we select the predictions over 1 – 75 AU as turbulence model 3's predictions and results from Bellamy et al. [6] are not available close to or after the HTS. Therefore, we separately include this figure to show apparent similarities and dissimilarities between observed and theoretical C_N^2 as a function of R.

The comparisons in Figure 6 show that predictions using the three turbulence amplitude models have similar radial trends, but there are differences in magnitude (especially, within 10 AU). Figure 6 also shows that data-driven values of C_N^2 using model 1 (red plus signs) and model 3 (black crosses) are larger than the theoretical predictions of model 3 (blue asterisks) and the results from Cairns [13] (green broken lines). Predictions of turbulence amplitude using model 2 and V2 data (blue asterisks) agree well with the results from Zank et al. [50] (magenta solid line).

Figure 7 shows the numerical predictions for the scattering angle $\theta_{SC}(R)$ using equation (26) for density turbulence models that use the data in Figures 2, 4, and 6 for plasma quantities, magnetic field, $l_i(R)$, and $C_N^2(R)$ as well as the analytic model of Cairns [13] using equation (29) that ignores inner scale effects and assumes a specific model for $C_N^2(R)$ (equation 28). Predictions for θ_{SC} employ the turbulence amplitudes for model 1 using equation (3)) and model 2 using equation (11). The figure also shows the apparent source sizes estimated by Cairns [13] from observations of roll modulations of the observed radiation near 33 kHz at $R \sim 18 AU$ [32] and $R \sim 45 - 48$ AU [28].

Figure 7 shows that the predictions are much higher than the observed θ_{SC} when $w = 1$, but that numerically and analytically predicted $\theta_{SC}(R)$ values become much closer to the observed θ_{SC} for $w = 0.01$. An immediate interpretation for the larger numerical estimates for $\theta_{SC}(R)$

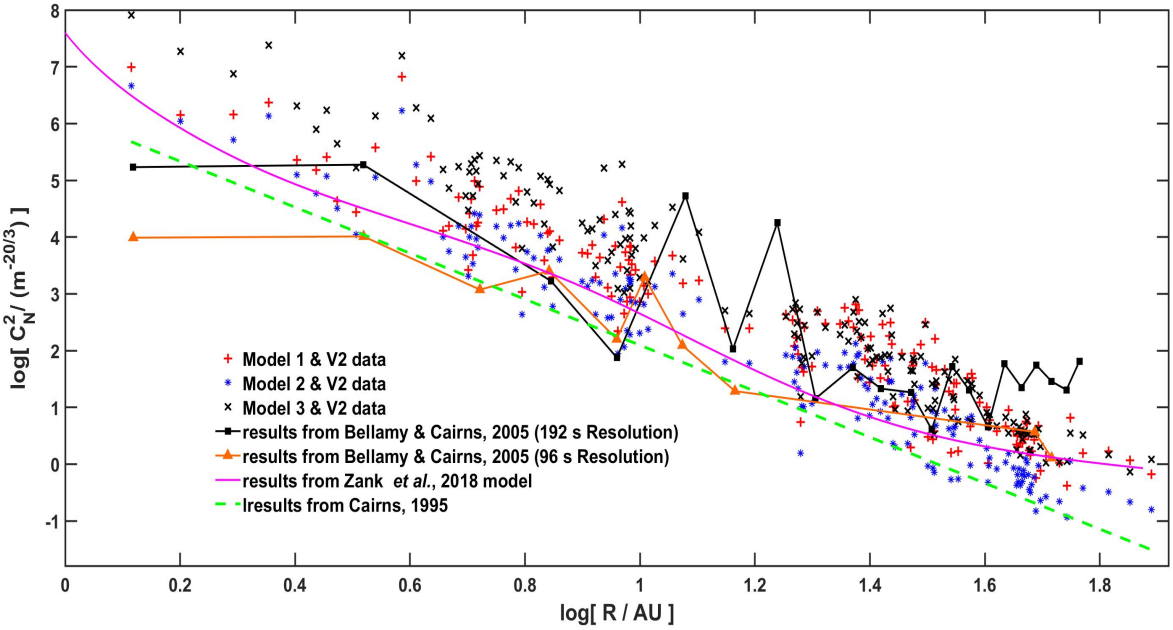

Figure 6. Comparison of predicted amplitudes C_N^2 using different models and V2 data from 1 AU to 75 AU. The red plus signs, the blue asterisks, and the black crosses present the V2 data driven C_N^2 using model 1, model 2, and model 3, respectively. The broken green line presents analytic predictions using equation (28) [13] whereas the magenta solid curve presents C_N^2 using Zank et al. [50]'s predictions. The black squares with a solid line and orange triangles with a solid line show C_N^2 from Bellamy et al. [6] for 192 s and 96 s resolutions, respectively.

from equation (26) is that the larger values of C_N^2 in the V2 data (Figure 6) yields larger values of $\theta_{SC}(R)$. However, this qualitative argument does not include the inner scale effects included in equation (26) via the term $q_i^{4-\alpha}$ with $l_i = q_i^{-1}$. Figure 8 demonstrates that the inner scale effect reduces the predicted $\theta_{SC}(R)$ by a factor ≈ 2.2 using equation (26) for the same $C_N^2(R)$ and comparing the predictions without inner scale effects (i.e., excluding $q_i^{4-\alpha}$ in equation (27)) included and the analytic θ_{SC} from Cairns [13]. We also included $w = 0.01$ like [13] for all predictions to reduce the value close to the observed θ_{SC}. Importantly, though inner scale effects are thus quantitatively important as argued previously by Armstrong et al. [4], they are not sufficient to bring the predicted and observed source sizes into close agreement.

Since the models in Figure 7 and 8 use Voyager density observations and theory appropriate to the slow solar wind relatively close to the ecliptic plane, it is possible that out-of-the-ecliptic effects are important. Specifically, the observations of radio waves by Gurnett et al. [28] were taken during the declining phase of the solar cycle when the spacecraft apparently was in the fast polar stream [8, 9, 37]. Moreover, more detailed consideration of the radio source region and the radiation's propagation to the observer [4, 19, 25] suggest that generation and propagation close to the ecliptic plane are unlikely. Crucially, the density variance is much stronger in the equatorial region than over the poles [4, 21], thereby yielding larger values of $\langle(\delta\rho)^2\rangle$, $C_N^2(R)$, and so $\theta_{SC}(R)$. We find in this paper that inner scale effects and the best available models for the near-eclipitc density turbulence yield scattering angles θ_{SC} that are much larger than those observed for the 2-3 kHz radiation. This provides a strong argument that out-of-the-ecliptic effects need to be incorporated complementing the earlier arguments of Armstrong et al. [4].

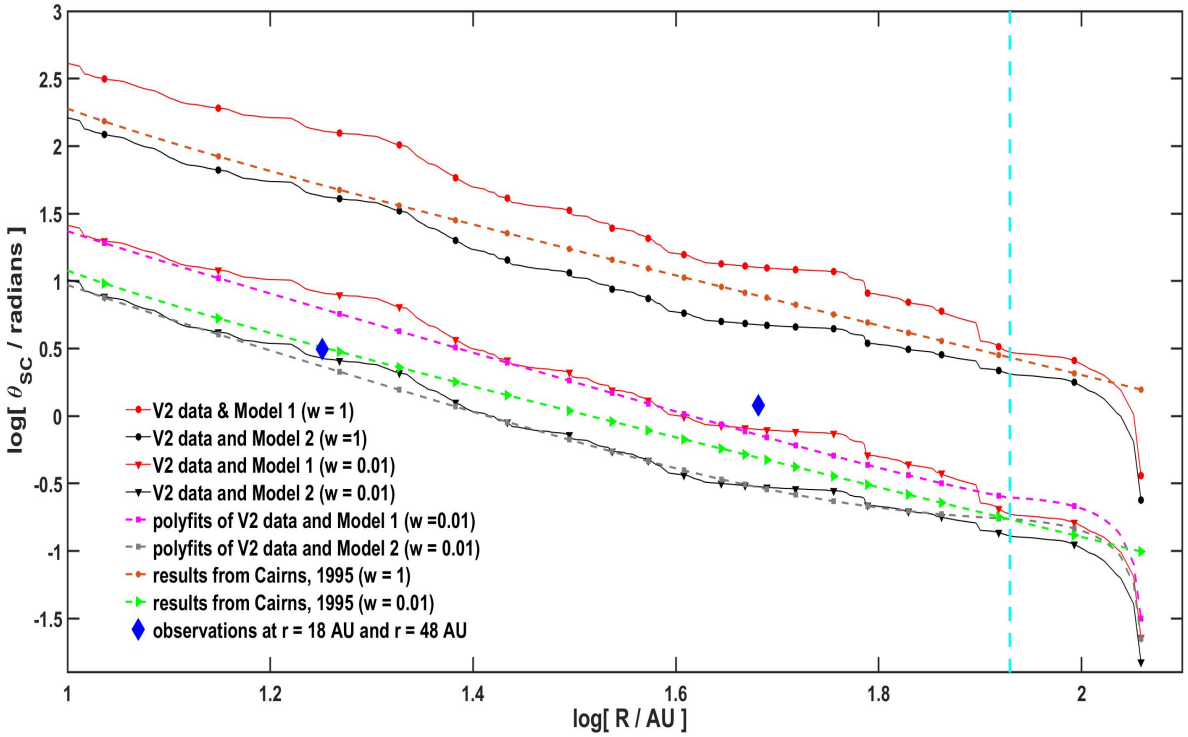

Figure 7. Radial variation of the scattering angle θ_{SC} predicted by equation (26) for various density turbulence models (curves) and estimates of the the observed source size (blue diamonds). Here dotted lines show the results for $w = 1$ and solid lines with triangles show the results for $w = 0.01$. The source is assumed to be at $R_{so} = 118$ AU and the frequency 3 kHz. The predictions use model 1 (red lines), model 2 (black lines) with V2 data for l_u, l_i, and $\langle(\delta\rho)^2\rangle$. The magenta broken lines with squares and gray broken lines with squares present θ_{SC} for polyfits to V2 data using model 1 and model 2, respectively. The brown dot-dashed lines and green lines with triangles show the analytic predictions for θ_{SC} of Cairns [13] for $w = 1$ and $w = 0.01$, respectively. The blue diamonds show the apparent source sizes from Cairns [13] using published roll modulation data for radiation near 3 kHz around $R \sim 18\,AU$ [32] and $R \sim 45 - 48\,AU$ [27]. The vertical broken cyan line is the same as Figures 4 and 5.

For now, though, like Cairns [13] we use a factor $w = 0.01$ to reduces $\theta_{SC}(R)$ to values that are in reasonable accord with the observations shown Figure 7. In the future, we plan to develop detailed models of polar density turbulence, evaluate the effect of latitudinal variations in detail, and assess whether these effects produce an effective value of $w \approx 0.01$ compared with in-ecliptic density turbulence.

6. Conclusions

The results from the foregoing analysis can be summarized as follows:

- We used three approaches (i.e. models 1, 2, and 3) to model $C_N^2(R)$ and Voyager 2 data. Predictions using models 1 and 2 show similar radial profiles from 1 AU to 118 AU, with a difference in magnitudes (Figure 5) due to the presence of of the term $\left[\ln\left(\frac{1}{k_{inj}l_u}\right)\right]^{-1}$ in equation (11) of model 2. We then compared $C_N^2(R)$ from 1 AU to 75 AU in Figure 6 using all three approaches together with the results derived from the turbulence transport models

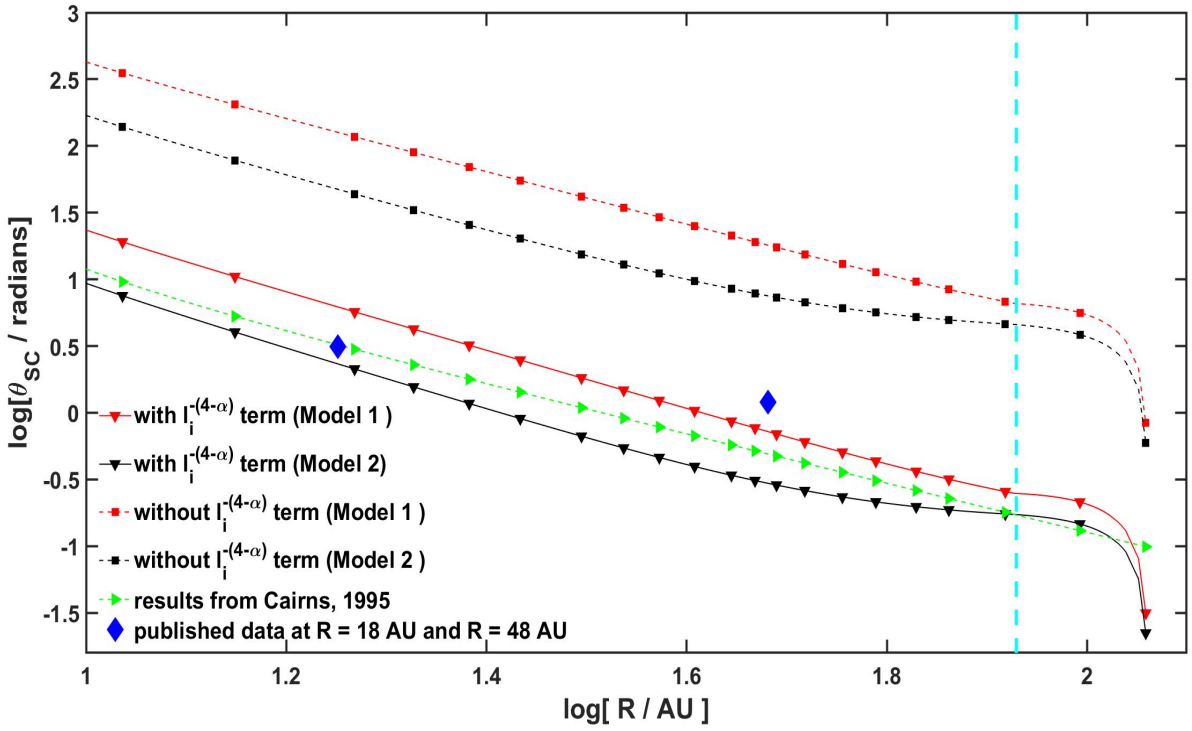

Figure 8. Radial variation of the scattering angle θ_{SC} predicted by using polyfits to V2 data and equation (26) with (solid lines with triangles) and without (broken lines with squares) the inner scale term ($q_i^{4-\alpha} = l_i^{-(4-\alpha)}$) for the density turbulence model 1 (red markers) and model 2 (black markers). The green broken line with triangles, blue solid diamonds, and vertical cyan line are same as in Figure 7. Here all results for θ_{SC} are multiplied by $w^{0.6}$ where $w = 0.01$.

of Zank et al. [49, 50], results from Bellamy et al. [6], and analytic predictions by Cairns [13]. The predictions using various models and V2 data all have similar radial trends on average, although with some quantitative differences. We also found that V2 data-driven predictions are 1 to 2 orders of magnitude larger than analytic C_N^2 by Cairns [13].

- We extended the theoretical model for $\theta_{SC}(R)$ by including an inner scale $l_i(R)$ for the turbulence and providing theoretical models for $l_i(R)$. The numerical results for $\theta_{SC}(R)$ employed C_N^2 from Figure 5 and l_i from Figure 4. Figure 7 shows that predicted values of θ_{SC} are much larger than the observed θ_{SC}, even with l_i included. This result indicates that we need to incorporate some missing physics in the investigation. Like Cairns [13], we introduced a factor $w = 0.01$ which allows us to a match the observations and models. Figure 7 shows that predicted values of $\theta_{SC}(R)$ when multiplied by $w^{0.6}$ agree reasonably well with Voyager derived observations of the source size. We used V2 data for the slow solar wind at the near-ecliptic plane, which cannot account for the factor $w \approx 0.01$ required to explain the observed radio source sizes.
- As a byproduct of the analysis, we found an important result about the scale at which turbulent energy is injected. As illustrated in Figure 3 (left panel), the turbulence transport model of Zank et al. [50] appears to describe the variance of the density fluctuations $\langle(\delta\rho)^2\rangle$ in the energy containing range quite well. To compute C_N^2, we use equation (11), which introduces the injection scale k_{inj}. Since $\langle(\delta\rho)^2\rangle$ is modeled accurately, we can use

the observed C_N^2 values to constrain k_{inj}. In doing so, we find quantitatively that k_{inj} corresponds to the solar rotation period. This is a quantitative demonstration of the well-known assumption that the largest scale injected into the turbulent energy of the solar wind corresponds to solar rotation.

In future, we will address in detail latitudinal variations of the density turbulence. This will include theoretical predictions for $C_N^2(R)$ and $l_i(R)$ for the polar and fast solar wind, prediction of $\theta_{SC}(R)$ as well as the scattering and propagation of the 2-3 kHz radio emissions.

Acknowledgments
We would like to thank CDAWeb and NASA for the Voyager data. We acknowledge the partial support of an NSF EPSCoR RIITrack-1 Cooperative Agreement OIA-1655280 and a NASA IBEX grant Sub0000167/80NSSC18K0237.

References

[1] L. Adhikari, G. P. Zank, R. Bruno, D. Telloni, P. Hunana, A. Dosch, R. Marino, and Q. Hu. The transport of low-frequency turbulence in astrophysical flows. II. solutions for the super-Alfvénic solar wind. *Astrophys. J.*, 805:63, 2015.

[2] L. Adhikari, G. P. Zank, D. Shiota P. Hunana and, R. Bruno, Q. Hu, and D. Telloni. II. transport of nearly incompressible magnetohydrodynamic turbulence from 1 to 75 AU. *Astrophys. J.*, 814:85, 2017.

[3] L. Adhikari, G. P. Zank, D. Telloni, P. Hunana, R. Bruno, and D. Shiota. Theory and Transport of Nearly Incompressible Magnetohydrodynamics Turbulence. III. Evolution of Power Anisotropy in Magnetic Field Fluctuations throughout the Heliosphere. *Astrophys. J.*, 851:117, 2017.

[4] J. W. Armstrong, W. A. Coles, and B. J. Rickett. Radio wave scattering in the outer heliosphere. *J. Geophys. Res.*, 105:5149–5156, 2000.

[5] S. D. Bale, M. J. Reiner, J. L. Bougeret J L, M. L. Kaiser, S. Krucker, D. E. Larson, and R. P. Lin. Can a charge-exchange induced density rise at the heliopause explain the frequency drift of the 3 kHz Voyager signal? *Geophys. Res. Lett.*, 26:1573–1576, 1999.

[6] B. R. Bellamy, I. H. Cairns, and C. W. Smith. Voyager spectra of density turbulence from 1 AU to the outer heliosphere. *J. Geophys. Res.*, 110:A10104, 2005.

[7] R. Bruno and V. Carbone. The solar wind as a turbulence laboratory. *Liv. Rev. Solar Phys.*, 10:208, 2013.

[8] L. F. Burlaga and N. F. Ness. Magnetic fields in the distant heliosphere approaching solar minimum: Voyager 1 and 2 observations during 1994. *J. Geophys. Res.*, 101:13473–13481, 1996.

[9] L. F. Burlaga and N. F. Ness. Global patterns of heliospheric magnetic field polarities and elevation angles: 1990 through 1995. *J. Geophys. Res.*, 102:19731–19742, 1997.

[10] L. F. Burlaga, N. F. Ness, M. H. Acüna, Y. M. Wang, N. R. Sheeley, C. Wang, and J. D. Richardson. Global structure and dynamics of large-scale fluctuations in the solar wind: Voyager 2 observations during 2005 and 2006. *J. Geophys. Res.*, 113:A02104, 2008.

[11] L. F. Burlaga, N. F. Ness, and J. D. Richardson. Heliosheath magnetic field and plasma observed by Voyager 2 during 2015 near solar maximum. *Astrophys. J.*, 816:9, 2018.

[12] I. H. Cairns. Fine structure in plasma waves and radiation near the plasma frequency in earth's foreshock. *J. Geophys. Res.*, 99:23505–23,513, 1994.

[13] I. H. Cairns. Radio wave scattering in the outer heliosphere: Preliminary calculations. *J. Geophys. Res. Lett.*, 22:3433–3436, 1995.

[14] I. H. Cairns. Angular broadening: effects of nonzero, spatially varying plasma frequency between the source and the observer. *Astrophys. J.*, 506:456–463, 1998.

[15] I. H. Cairns and S. A. Fuselier. The plasma depletion layer beyond the heliopause: Evidence, implications, and predictions for Voyager 2 and New Horizons. *Astrophys. J.*, 834:197 (pp 11), 2017.

[16] I. H. Cairns and S. A. Fuselier. Electron and ion heating due to magnetic reconnection at the heliopause. *J. Phys.: Conf. Series*, 1100:article id. 012004, 2018.

[17] I. H. Cairns and D. A. Gurnett. Outer heliospheric radio emissions: 1. constraints on emission processes and the source region. *J. Geophys. Res.*, 97:6235–6244, 1992.

[18] I. H. Cairns and Donald A. Gurnett. Outer heliospheric radio emissions 1. constraints on emission processes and the source region. *J. Geophys. Res.*, 97:6245–6249, 1992.

[19] I. H. Cairns and G. P. Zank. Turn-on of 2–3 kHz radiation beyond the heliopause. *Geophys. Res. Letts.*, 29:1143, 2002.

[20] I. H. Cairns, Williams S. Kurth, and Donald A. Gurnett. Outer heliospheric radio emissions 2. foreshock source models. *J. Geophys. Res.*, 97:6245–6249, 1992.

[21] W. A. Coles. Interplanetary scintillation observations of the high-latitude solar wind. *Space Sci. Rev.*, 72:211, 1995.

[22] W. A. Coles, R. G. Frehlich, B. J. Rickett, and J. L. Codona. Refractive scintillation in the interstellar medium. *Astophys. J.*, 315:666–674, 1987.

[23] A. Czechowski and S. Grzedzielski. Can a charge-exchange induced density rise at the heliopause explain the frequency drift of the 3 kHz Voyager signal? *Geophys. Res. Lett.*, 21: 2777–2780, 1994.

[24] N. Eugene Engelbrecht and R. Du Toit Strauss. A tractable estimate for the dissipation range onset wavenumber throughout the heliosphere. *Astrophys. J.*, 856:159, 2018.

[25] S. A. Fuselier and Iver H. Cairns. Plasma properties at the Voyager 1 crossing of the heliopause. *J. Phys.: Conf. Series*, 642:article id. 012010, 2015.

[26] D. A. Gurnett. Heliospheric radio emissions. *Space Sci. Rev.*, 72:243–254, 1995.

[27] D. A. Gurnett, W. S. Kurth, S. C. Allendoff, and R. L. Poynter. Radio emission for the heliopause triggered by an interplanetary shock. *Science*, 262:199–203., 1993.

[28] D. A. Gurnett, S.C. Allendoff, and W. S. Kurth. Direction finding measurement of heliospheric 2-3 kHz radio emissions. *Geophys. Res. Left.*, 25:4433–4436., 1998.

[29] D. A. Gurnett, W. S. Kurth, L. F. Burlaga, and N. F. Ness. Heliospheric radio emissions. *Science*, 341:1489–1492, 2013.

[30] J. V. Hollweg. Angular broadening of radio sources by solar wind turbulence. *J. Geophys. Res.*, 75:3715, 1970.

[31] M. Ingale, P. Subramanian, and I. Cairns. Coronal turbulence and the angular broadening of radio sources - the role of the structure function. *Mon. Not. R. Astron. Soc.*, 447:3486–3497, 2015.

[32] W. S. Kurth. The low frequency interplanetary radio emission: evidence of the solar wind-interstellar wind interaction? *in Proc. of the Sixth International Solar Wind Conference, Vol. II, edited by V. J. Pizzo, T. E. Holzer, and D. G. Sime*, page 667, 1988.

[33] W. S. Kurth, D. A. Gurnett, F. L. Scarf, and R. L. Poynter. Detection of a radio emission at 3 kHz in the outer heliosphere. *Nature*, 312:27–31, 1984.

[34] L. C. Lee. Wave propagation in a random medium: A complete set of the moment equations with different wavenumbers. *J. Math. Phys.*, 14:1431, 1974.

[35] L. C. Lee. Wave propagation in a random medium: A complete set of the moment equations with different wavenumbers. *J. Math. Phys.*, 14:1431, 1994.

[36] L. C. Lee and J.R. Jokipii. Strong scintillations in astrophysics. i. the markov approximation, its validity and application to angular broadening. *Astrophys. J.*, 196:695, 1975.

[37] N. F. Ness and L. F. Burlaga. Merged interaction regions and large scale fluctions observed by Voyager 1 and 2 in the distance heliosphere, in *solar wind eight*, edited by D. Winterhalter *et al. AIP Conf. Proc.*, 382:591–594, 1996.

[38] B. J. Rickett. Evidence of scattering effects on the sizes of interplanetary type iii radio bursts. *Ann. Rev. Astron. Astrophys.*, 15:479, 1977.

[39] B. J. Rickett. Interstellar scattering and scintillation of radio waves. *Ann. Rev. Astron. Astrophys.*, 15:479–504, 1977.

[40] C. W. Smith, B. J. Vasquez, and J. V. Hollweg. Observational constraints on the role of cyclotron damping and kinetic Alfvén waves in the solar wind. *Astrophys. J.*, 745:8, 2012.

[41] J. L. Steinberg, S. Hoang, and G.A. Dulk. Evidence of scattering effects on the sizes of interplanetary type iii radio bursts. *Astron. Astrophys.*, 150:205, 1985.

[42] E. C. Stone, A. C. Cummings, N. Lal F. B. McDonald, B. C. Heikkila, and W. R. Webber. Voyager 1 explores the termination shock region and the heliosheath beyond. *Science*, 309: 2017, 2005.

[43] E. C. Stone, A. C. Cummings, F. B. McDonald, B. C. Heikkila, N. Lal, and W. R. Webber. An asymmetric solar wind termination shock. *Nature*, 454:71, 2008.

[44] E. C. Stone, A. C. Cummings, F. B. McDonald, B. C. Heikkila, N. Lal, and W. R. Webber. Voyager 1 observes low-energy galactic cosmic rays in a region depleted of heliospheric ions. *Science*, 341:150, 2013.

[45] G. P. Zank. Interaction of the solar wind with the local interstellar medium: a theoretical perspective. *Space Sci. Rev.*, 89:413–688, 1999.

[46] G. P. Zank. *Transport Processes in Space Physics and Astrophysics*. Springer-Verlag New York, New York, USA, 2014.

[47] G. P. Zank. Faltering Steps Into the Galaxy: The Boundary Regions of the Heliosphere. *Annu. Rev. Astron. Astrophys.*, 53:449–500, 2015.

[48] G. P. Zank, I. H. Cairns, D. J. Donohue, and W. H. Matthaeus. Radio emissions and the heliospheric termination shock. *J. Geophys. Res.*, 99:14729, 1994.

[49] G. P. Zank, L. Adhikari, P. Hunana, D. Shiota, R. Bruno, and D. Telloni. Theory and transport of nearly incompressible magnetohydrodynamic turbulence. *Astrophys. J.*, 835: 147, 2017.

[50] G. P. Zank, L. Adhikari, L.-L. Zhao, P. Mostafavi, E. J. Zirnstein, and D. J. McCommas. The pickup ion-mediated solar wind. *Astrophys. J.*, 869:23, 2018.

[51] L.-L Zhao, L. Adhikari, , G. P. Zank, Q. Hu, and X. S. Feng. Influence of the solar cycle on turbulence properties and cosmic-ray diffusion. *Astrophys. J.*, 854:94, 2018.